Thermoelectric transport properties in 3D Dirac semimetal Cd$_3$As$_2$

R Amarnath[1], K S Bhargavi[1] and S S Kubakaddi[2]

[1] Department of Physics, Siddaganga Institute of Technology, Tumakuru 572 103, Karnataka, India
[2] Department of Physics, K L E Technological University, Hubballi 580 031, Karnataka, India

E-mail: bhargaviks@sit.ac.in

CrossMark

Abstract

Thermoelectric transport properties, namely, electrical conductivity, electronic thermal conductivity, and diffusion thermopower are theoretically investigated in 3D Dirac semimetal Cd$_3$As$_2$. We employ Boltzmann transport formalism and consider the electron scattering by charged impurities, short-range disorder, acoustic phonons, and optical phonons. The Boltzmann transport equation is solved using the Ritz iteration technique to obtain the first-order perturbation distribution function for the interaction of electrons with inelastic polar optical phonons scattering. The numerical results are presented in the temperature range 2–300 K with the electron concentration in the range $(0.1–10) \times 10^{18}$ cm^{-3}. It is found that, at low temperature $< {\sim}70$ K transport coefficients are dominated by charged impurity scattering and at higher temperature the phonon scattering is found to be dominant. The validity of Wiedemann–Franz law is examined. Recently observed experimental results are explained by our theory.

(Some figures may appear in colour only in the online journal)

1. Introduction

The study of materials with linear energy dispersion relation in both two (2D)- and three (3D)-dimensional materials is one of the most active areas of research in condensed matter physics. Graphene is one such 2D material which has been studied exhaustively in last one and half decade [1, 2]. In 3D materials, the three-dimensional Dirac semimetals (3DDS), Weyl semimetals (WS), and topological insulators (TI) are the ones which gained interest in recent years. The surge of current research interest has focused on recently discovered novel 3DDS [3–18], which are interesting from the point of view of fundamental physics and their massive applications in future technological developments, particularly those relating to high electron mobility [7] and better optical properties [19].

The Angle-resolved photoemission spectroscopy measurements gave evidence for the existence of 4-fold degenerate Dirac points in Cd$_3$As$_2$ [8, 9], and A$_3$Bi (A = Na, K, Rb) materials which were theoretically predicted [4, 6]. These

materials have revealed the linear electron energy dispersion [3, 7] around Dirac points making gapless energy bands. Of the available 3DDS materials, Cd$_3$As$_2$ has received great attention because of their chemical stability [8, 13] and very large electron mobility at very low temperature [14–16]. The recent reports of magneto-transport properties reveal a remarkably ultra-high in-plane Fermi velocity of 1.5×10^6 m s^{-1} [16, 17], and a large room temperature mobility of the order $\sim 10^4$ cm^2 V^{-1} s^{-1} [12]. The experimental investigation of Zhao *et al* [14] shows a quite low residual resistivity of about 11.6 nΩ cm at 6 K, Liang *et al* [15] also observed a very low resistivity of few tens of nΩ cm with a ultra-high mobility of 9×10^6 cm^2 V^{-1} s^{-1} at 5 K in one of their samples. These observed results showcase the suppression of backscattering at low temperature. The zero magnetic field resistivity and quantum transport properties in a magnetic field of 3DDS Cd$_3$As$_2$ are reported by He *et al* [18]. In an ideal Cd$_3$As$_2$, with a Fermi level close to the Dirac point, a large linear quantum magnetoresistance (up to 3100%) has been observed [20].

Thus, these interesting results in 3DDS Cd_3As_2 motivate us to address the other transport properties namely, thermoelectric properties.

The study of thermoelectric properties involves a study of electrical and thermal responses of these materials to the electric field and temperature gradient. The thermoelectric energy conversion efficiency depends upon the performance of the materials that is quantified by the dimensionless factor known as thermoelectric figure-of-merit, $Z = S^2\sigma/\kappa$, where S is the Seebeck co-efficient, σ is the electrical conductivity and κ is thermal conductivity of the material [21]. The study of thermopower/Seebeck co-efficient is a measure of the magnitude of induced thermoelectric voltage in response to temperature gradient. There are two contributions to S: diffusion thermopower S^d and phonon drag thermopower S^g. S^d is found to be important at relatively higher temperature [21]. The thermal conductivity κ involves the study of contribution from both electrons (κ_e) and phonons (κ_{ph}). κ_e is expected to be important in the samples with high electron concentrations and relatively at higher temperature [22]. The material with large power factor $S^2\sigma$ with low κ would enhance the value of Z.

A rigorous study of these thermoelectric properties has drawn much attention in recent years because it is expected to play a significant role in meeting the energy challenges of the future [23, 24]. The study not only provides a means of assessing the efficiency of thermoelectric devices but also a non-destructive technique to understand the carrier scattering mechanisms operative in the system. The 3DDS Cd_3As_2 is a material of current interest whose thermoelectric properties need to be investigated.

In 3DDS Cd_3As_2, Zhang *et al* [25] have reported an unexpected low thermal conductivity of 4.17 Wm^{-1} K^{-1} and $S = -74.1$ μV K^{-1} at 300 K along with a large power factor of 1.58 mW·m^{-1} K^{-2} at room temperature. Wang *et al* [26] have measured σ, S and κ for four samples with different carrier concentrations in zero and non-zero magnetic field for $T = \sim 5$–500 K. In zero magnetic field, S is found to increase almost linearly with increasing temperature. The thermal conductivity is found to decrease rapidly with increasing temperature for $T < \sim 50$ K and remains nearly constant/moderately increasing for temperature up to 300–400 K. For higher T it is found to increase. Pariari *et al* [27] observe a linear temperature dependence of S over a wide range with $S = -60$ μV K^{-1} at 300 K in zero magnetic field. A good agreement with the Mott relation is obtained by tuning the energy dependence of the relaxation time.

Das Sarma *et al* [11] have developed a theory of electrical conductivity, σ, considering scattering from the screened Coulomb disorder due to random charged impurities. Also, acoustic phonon limited σ is briefly discussed in Bloch–Grüneisen (BG) and equipartition (EP) regime. Lundgren *et al* [10] have theoretically studied electrical conductivity, electronic thermal conductivity and thermopower using the Boltzmann transport equation (BTE) technique in the relaxation time approximation, in the presence of the magnetic field, ignoring the scattering by phonons. Zhou *et al* [28] have presented the First principle calculations of the electronic structure and the thermoelectric properties, by using

simple thermoelectric relations, in Cd_3As_2 doped with both n and p-type impurities. Their calculations are based on the Boltzmann transport theory reserving the contributions from various scattering mechanisms and their relative importance. One of the authors [29] has presented the detailed calculations of the mobility limited by acoustic and optical phonons by solving the BTE in relaxation time approximation and recent experimental results are explained. In large electron concentration Cd_3As_2, the scattering by phonons is considered to be quasi-elastic.

In this article, we have studied thermoelectric transport coefficients considering scattering from charged impurities (CI), short-range disorders (SD), acoustic (AP) and optical (OP) phonons in 3DDS Cd_3As_2. A theory of solving semiclassical BTE by Ritz iteration technique for 3D Dirac system is presented in section 2. It is followed by the theory of thermoelectric transport properties, namely electrical conductivity, electronic thermal conductivity and diffusion thermopower in Cd_3As_2. In section 3, we have investigated the relative contribution and importance of the electron scattering by various scattering mechanisms. Our calculations are compared with the experimental observations.

2. Theoretical formulation

The carriers in 3DDS Cd_3As_2 behave like Dirac fermions. For low energy excitations, the electron energy dispersion is assumed to be isotropic and linear. It is given by $E_{\mathbf{k}} = \pm s\hbar v_F|\mathbf{k}|$, where s is the band index and it takes the value ± 1 for conduction and valance band, $\mathbf{k}$ is the 3D electron wave vector, and v_F is the Fermi velocity. The corresponding ground state wave function for 3D carriers is given by [11],

$$\psi_{\mathbf{k}}^s(E_{\mathbf{k}}) = \frac{1}{\sqrt{2V}} \exp(i\mathbf{k} \cdot \mathbf{r})\chi^s \quad (1)$$

where V is the sample volume, $\mathbf{r} = (x, y, z)$, $\chi^{\pm} = [\cos(\theta_{\mathbf{k}}/2) \pm \sin(\theta_{\mathbf{k}}/2)\, e^{i\varphi}]^T$ and $\theta_{\mathbf{k}}$ (φ) is the polar (azimuthal) angle in 3D $\mathbf{k}$ space. We consider the situation in which Fermi energy E_F is much above the Dirac point.

2.1. Boltzmann transport equation (BTE)

The probability occupation of an electron in state $\mathbf{k}$ is given by the distribution function $f(E_{\mathbf{k}})$. In the presence of an electric field $\boldsymbol{E}$ and temperature gradient ∇T, electron distribution function $f(E_{\mathbf{k}})$ experiences a perturbation and hence deviates from its equilibrium value $f_0(E_{\mathbf{k}})$. This deviation from the equilibrium value can be obtained by a series expansion of the Legendre polynomial. For low electric field and temperature gradient, neglecting the higher-order terms in $\boldsymbol{E}$ and ∇T, the series can be expanded as [30]

$$f(E_{\mathbf{k}}) = f_0(E_{\mathbf{k}}) + f_1(E_{\mathbf{k}}) \quad (2)$$

where $f_1(E_{\mathbf{k}}) = -Fv_{\mathbf{k}} \cos\theta_{\mathbf{k}}\, (\partial f_0(E_{\mathbf{k}})/\partial E_{\mathbf{k}})\, \Phi(E_{\mathbf{k}})$ is the first-order perturbation term in the distribution function due to external fields. Here $\boldsymbol{F} = [-e\boldsymbol{E} + ((E_{\mathbf{k}} - E_F)/T)(-\nabla T)]$ is force acting on electrons due to $\boldsymbol{E}$ and ∇T, $v_{\mathbf{k}}$ is the velocity

of the carriers in state $\mathbf{k}$, θ_k is the angle between $\boldsymbol{F}$ and $\mathbf{k}$, E_F is the Fermi energy and $\Phi(E_{\mathbf{k}})$ is the perturbation function (to be determined).

The rate of change of $f(E_{\mathbf{k}})$ with respect to time t is given by the BTE [31]

$$\frac{\mathrm{d}f}{\mathrm{d}t} = -\frac{1}{\hbar}\frac{\partial E_{\mathbf{k}}}{\partial \mathbf{k}} \cdot \frac{\partial f}{\partial \mathbf{r}} - \frac{eE}{\hbar} \cdot \frac{\partial f}{\partial \mathbf{k}} + I_c(f), \quad (3)$$

where $I_c(f)$ is the collision integral arising due to the scattering of an electron from state $\mathbf{k}$ to $\mathbf{k'}$ and is given by

$$I_c(f) = -\frac{1}{8\pi^3}\int [S(\mathbf{k}, \mathbf{k'})f(E_{\mathbf{k}})(1 - f(E_{\mathbf{k'}}))$$
$$-S(\mathbf{k'}, \mathbf{k})f(E_{\mathbf{k'}})(1 - f(E_{\mathbf{k}}))]\mathrm{d}\mathbf{k'}. \quad (4a)$$

Here $S(\mathbf{k}, \mathbf{k'})$ is the differential scattering rate from $\mathbf{k}$ to $\mathbf{k'}$. In the steady-state, the Boltzmann equation becomes

$$I_c(f) = \frac{1}{\hbar}\frac{\partial E_{\mathbf{k}}}{\partial \mathbf{k}} \cdot \frac{\partial f}{\partial \mathbf{r}} + \frac{eE}{\hbar} \cdot \frac{\partial f}{\partial \mathbf{k}}. \quad (4b)$$

Using the principle of detailed balance, $[S(\mathbf{k}, \mathbf{k'})\, f_0(E_{\mathbf{k}})(1 - f_0(E_{\mathbf{k'}}))] = [S(\mathbf{k'}, \mathbf{k})\, f_0(E_{\mathbf{k'}})\,(1 - f_0(E_{\mathbf{k}}))]$, then collision integral $I_c(f)$ for 3D Dirac carriers can be written as

$$I_c(f) = -\frac{1}{8\pi^3}\frac{Fv_F}{k_B T}\cos\theta_k \int [S(\mathbf{k}, \mathbf{k'})f_0(E_{\mathbf{k}})(1 - f_0(E_{\mathbf{k'}}))$$
$$\times [\Phi(E_{\mathbf{k}}) - \cos\theta\,\Phi(E_{\mathbf{k'}})]\mathrm{d}\mathbf{k'}, \quad (5)$$

where θ is the angle between $\mathbf{k}$ and $\mathbf{k'}$. Substituting the above expressions in equation (4b), we arrive at the linearized BTE for the 3D Dirac carriers and is given by

$$1 = \sum_{\mathbf{k'}} [\Phi(E_k) - \cos\theta\,\Phi(E_{\mathbf{k'}})]S(\mathbf{k}, \mathbf{k'})\frac{1 - f_0(E_{\mathbf{k'}})}{1 - f_0(E_{\mathbf{k}})}. \quad (6)$$

For elastic and quasi-elastic scattering, $\Phi(E_{\mathbf{k}}) = \Phi(E_{\mathbf{k'}})$ and it turns out be momentum relaxation time $\tau(E_{\mathbf{k}})$ ($=\Phi(E_{\mathbf{k}})$), for these scatterings [31].

2.2. Scattering theory in 3DDS

In this section, we find $\Phi(E_{\mathbf{k}})$ for the electron scattering, in 3DDS Cd$_3$As$_2$, from the charged impurities, short-range disorders, and acoustic and optical phonons. The scattering of electrons by charged impurities and short-range disorders is elastic. Scattering by acoustic phonons via deformation potential coupling is assumed to be quasi-elastic and that by optical phonons to be inelastic. These scattering processes are effective at different lattice temperatures namely impurity scattering for relatively pure samples dominates at low temperatures while polar optical phonons important at high temperatures. On the other hand, scattering by acoustic phonons is important for intermediate temperatures.

2.2.1. Scattering by charged impurities (CI).

We assume that the charged impurities are randomly spread in the material with impurity concentration n_i. These charged impurities are screened by intrinsic free Dirac electrons and hence the interaction potential becomes screened coulomb disorder. Using equation (6), the energy-dependent electron scattering time $\tau_{CI}(E_{\mathbf{k}})$, in 3D Dirac material, due to CI scattering within the Born approximation is given by [11]

$$\frac{1}{\tau_{CI}(E_{\mathbf{k}})} = \frac{n_i E_{\mathbf{k}}^2}{2\pi\hbar^4 v_F^3}\int_0^\pi \left|\frac{V(\mathbf{k}, \mathbf{k'})}{\varepsilon(q, T)}\right|^2 \sin\theta(1 - \cos\theta)\left(\frac{1 + \cos\theta}{2}\right)\mathrm{d}\theta \quad (7)$$

where $V(\mathbf{k}, \mathbf{k'}) = (4\pi e^2/\varepsilon_s)\,(1/q^2)$ is the 3D Fourier transform of the Coulomb potential, ε_s is the background dielectric constant of the material, $\varepsilon(q, T) = \{1 + [q_{TF}(T)/q]^2\}$ [11] is the static dielectric function, $q_{TF}(T) = (4\pi e^2 D(E_F)/\varepsilon_s) [1 - (\pi^2/6)(T/T_F)^2]$ is the Thomas-Fermi (TF) wave vector, $D(E_{\mathbf{k}}) = g E_{\mathbf{k}}^2/(2\pi^2(\hbar v_F)^3)$ is the density of states, $g = g_s g_v$ is the total degeneracy and T_F is the Fermi temperature. The equation for $q_{TF}(T)$, given here, is valid for $T < T_F$. The relaxation time is evaluated in the long-wavelength limit with the temperature-dependent TF screening. It is to be noted that for elastic and quasi-elastic scattering (i.e. in equations (7), (8) and (10)) $q = 2k\sin(\theta/2)$.

2.2.2. Scattering by short-range disorders (SD).

SDs are the finite range potential caused by the defects or dislocations present in the material. Taking $n_d V_o^2$ as the effective potential experienced by charge carriers with defects concentration n_d, the energy dependent relaxation time due to SD scattering is shown to be [11]

$$\frac{1}{\tau_{SD}(E_{\mathbf{k}})} = \frac{n_d V_0^2 E_{\mathbf{k}}^2}{2\pi\hbar^4 v_F^3}\int_0^\pi \frac{\sin\theta}{|\varepsilon(q, T)|^2}(1 - \cos\theta)\left(\frac{1 + \cos\theta}{2}\right)\mathrm{d}\theta. \quad (8)$$

2.2.3. Scattering by acoustic phonons (AP).

In 3DDS Cd$_3$As$_2$, for E_F much above the Dirac point, the Fermi energy $E_F \gg \hbar\omega_q$, the acoustic phonon energy, and scattering can be treated as quasi-elastic. Then from equation (6), the solution for $\Phi(E_{\mathbf{k}})$ gives momentum relaxation time $\tau_{AP}(E_{\mathbf{k}})$, as found in conventional 3D semiconductors [32], for acoustic phonon scattering in 3DDS. The equation for $\tau_{AP}(E_{\mathbf{k}})$ is given by

$$\frac{1}{\tau_{AP}(E_{\mathbf{k}})} = \sum_{\mathbf{k'}} S(\mathbf{k}, \mathbf{k'})(1 - \cos\theta)\frac{1 - f_0(E_{\mathbf{k'}})}{1 - f_0(E_{\mathbf{k}})} \quad (9)$$

with the scattering probability between the states, $\mathbf{k}$ and $\mathbf{k'}$ given by $S(\mathbf{k}, \mathbf{k'}) = (2\pi/\hbar) \sum_q |M_{\mathbf{kk'}}|^2 \Delta(E_{\mathbf{k}}, E_{\mathbf{k'}})$, where $|M_{\mathbf{kk'}}|^2$ is the interaction matrix element and $\Delta(E_{\mathbf{k}}, E_{\mathbf{k'}}) = [N_q\,\delta(E_{\mathbf{k}} - E_{\mathbf{k'}} + \hbar\omega_q) + (N_q + 1)\,\delta(E_{\mathbf{k}} - E_{\mathbf{k'}} - \hbar\omega_q)\,\theta(E_{\mathbf{k}} - \hbar\omega_q)]$. Here first and the second terms are, respectively, for the absorption and emission of phonon with wave vector q and energy $\hbar\omega_q = \hbar v_{ph}q$, where v_{ph} being the acoustic phonon velocity, $\theta(E_{\mathbf{k}} - \hbar\omega_q)$ is the step function and $N_q = [\exp(\hbar\omega_q/k_B T) - 1]^{-1}$ is the phonon occupation factor.

The screened electron–phonon interaction matrix element is given by $|M_{\mathbf{kk'}}|^2 = |C(q)|^2/|\varepsilon(q, T)|^2$. For electron scattering via acoustic deformation potential coupling $|C(q)|^2 = (D^2\hbar q/2V\rho_m v_{ph})[(1 + \cos\theta)/2]$, where D is the deformation potential coupling constant (which signifies the strength of electron–phonon scattering), ρ_m is the mass density, and $[(1 + \cos\theta)/2]$ is the factor arising due to the chiral nature of the Dirac electrons in 3DDS. Using this matrix element in equation (9), the $\tau_{AP}(E_{\mathbf{k}})$ is found to be,

$$\frac{1}{\tau_{AP}(E_{\mathbf{k}})} = \frac{D^2}{4\pi\rho_m v_{ph}(\hbar v_F)^3} \frac{1}{(1-f_0(E_{\mathbf{k}}))}$$
$$\times \int_0^\pi \frac{q\sin\theta(1-\cos\theta)[(1+\cos\theta)/2]}{|\varepsilon(q,T)|^2}$$
$$\times[(E_{\mathbf{k}}+\hbar\omega_q)^2 N_q(1-f_0(E_{\mathbf{k}}+\hbar\omega_q))$$
$$+(E_{\mathbf{k}}-\hbar\omega_q)^2(N_q+1)(1-f_0(E_{\mathbf{k}}-\hbar\omega_q))]\mathrm{d}\theta. \qquad (10)$$

2.2.4. Scattering by polar optical phonons (OP). Since the electron scattering by OPs is inelastic, equation (6) has to be solved for $\Phi(E_{\mathbf{k}})$ without any approximation. Amongst several techniques existing in the literature, the Ritz iteration technique has been found to be very convenient because of its auto-correction of the errors and accuracy [30]. Kawamura and Das Sarma [31] have used the Ritz iteration technique to solve BTE in conventional 2D heterostructures with the parabolic energy dispersion relation. In the present work, we solve the 3D linearized BTE for three-dimensional Dirac system with linear energy dispersion relation following the Ritz iteration method and hence obtain the perturbation function $\Phi(E_{\mathbf{k}})$ for inelastic scattering by polar optical phonons. The matrix element for electron-optical phonon interaction via Fröhlich coupling is given by $|C(q)|^2 = (2\pi e^2\hbar\omega_0/Vq^2)(1/\varepsilon_\infty - 1/\varepsilon_s)[(1+\cos\theta)/2]$ [29, 33, 39], where $\hbar\omega_0$ is the optical phonon energy, and ε_s (ε_∞) is the static (optical) dielectric constant of the material.

Substituting the above matrix element in equation (6), the linearized BTE can be written in the form of an equation coupling $\Phi(E_{\mathbf{k}})$ with $\Phi(E_{\mathbf{k}}\pm\hbar\omega_0)$,

$$1 = S_0(E_{\mathbf{k}})\Phi(E_{\mathbf{k}}) - S_a(E_{\mathbf{k}})\Phi(E_{\mathbf{k}}+\hbar\omega_0) \\ -S_e(E_{\mathbf{k}})\Phi(E_{\mathbf{k}}-\hbar\omega_0), \qquad (11)$$

where $S_0(E_{\mathbf{k}})$ is the sum of in and out scattering contributions of elastic and quasi-elastic scattering processes and sum of in and out scattering contributions from OPs. The other terms $S_a(E_{\mathbf{k}})$ and $S_e(E_{\mathbf{k}})$ denote the in scattering contributions from the inelastic scattering process due to OPs. These functions are given by

$$S_0(E_{\mathbf{k}}) = \frac{e^2\omega_0}{(\hbar v_F)^3}\left(\frac{1}{\varepsilon_\infty}-\frac{1}{\varepsilon_s}\right)\frac{1}{1-f_0(E_{\mathbf{k}})}$$
$$\times[(E_k+\hbar\omega_0)^2(1-f_0(E_{\mathbf{k}}+\hbar\omega_0))N_0 I_+(E_{\mathbf{k}})$$
$$+(E_{\mathbf{k}}-\hbar\omega_0)^2(1-f_0(E_{\mathbf{k}}-\hbar\omega_0))(N_0+1)I_-(E_{\mathbf{k}})$$
$$\theta(E_{\mathbf{k}}-\hbar\omega_0)]+\tau_{tot}^{-1}(E_{\mathbf{k}}), \qquad (12a)$$

$$S_a(E_{\mathbf{k}}) = \frac{e^2\omega_0}{(\hbar v_F)^3}\left(\frac{1}{\varepsilon_\infty}-\frac{1}{\varepsilon_s}\right)\frac{1}{1-f_0(E_{\mathbf{k}})}$$
$$\times[(E_{\mathbf{k}}+\hbar\omega_0)^2(1-f_0(E_{\mathbf{k}}+\hbar\omega_0))N_0 J_+(E_{\mathbf{k}})] \qquad (12b)$$

and

$$S_e(E_{\mathbf{k}}) = \frac{e^2\omega_0}{(\hbar v_F)^3}\left(\frac{1}{\varepsilon_\infty}-\frac{1}{\varepsilon_s}\right)\frac{1}{1-f_0(E_{\mathbf{k}})}$$
$$\times[(E_{\mathbf{k}}-\hbar\omega_0)^2(1-f_0(E_{\mathbf{k}}-\hbar\omega_0)) \qquad (12c)$$
$$\times(N_0+1)J_-(E_{\mathbf{k}})\theta(E_{\mathbf{k}}-\hbar\omega_0)],$$

where $\tau_{tot}^{-1}(E_{\mathbf{k}}) = \tau_{AP}^{-1}(E_{\mathbf{k}}) + \tau_{CI}^{-1}(E_{\mathbf{k}}) + \tau_{SD}^{-1}(E_{\mathbf{k}})$. The integrals

$$I_\pm(E_{\mathbf{k}}) = \int_0^\pi \frac{\sin\theta}{q_\pm^2(E_{\mathbf{k}},\theta)}\frac{[(1+\cos\theta)/2]}{|\varepsilon(q_\pm,T)|^2}\mathrm{d}\theta \qquad (13a)$$

and

$$J_\pm(E_{\mathbf{k}}) = \int_0^\pi \frac{\sin\theta\cos\theta}{q_\pm^2(E_{\mathbf{k}},\theta)}\frac{[(1+\cos\theta)/2]}{|\varepsilon(q_\pm,T)|^2}\mathrm{d}\theta \qquad (13b)$$

represent the angular dependence of the electron–phonon interactions with $q_\pm^2(E_{\mathbf{k}},\theta) = [(1/\hbar v_F)^2 (E_{\mathbf{k}}^2 + (E_{\mathbf{k}}\pm\hbar\omega_0)^2 - 2E_{\mathbf{k}}(E_{\mathbf{k}}\pm\hbar\omega_0)\cos\theta)]$ and $+(-)$ sign denotes the phonon emission (absorption).

Here, we employ a Ritz iterative technique [34] and obtain the solution for $\Phi(E_{\mathbf{k}})$ as follows. For a given value of the electron energy $E_{\mathbf{k}} = E_j + n\hbar\omega_0$, where $0 < E_j < \hbar\omega_0$ and $n = 0$, 1, 2…, in the first step of this iteration method, we set $S_a(E_{\mathbf{k}})$ and $S_e(E_{\mathbf{k}})$ equal to zero in equation (11), so that zeroth-order solutions are given by

$$\Phi^0(E_j + n\omega_0) = S_0^{-1}(E_j + n\hbar\omega_0) \qquad (14a)$$

and

$$\Phi^0(E_j + (n\pm 1)\hbar\omega_0) = S_0^{-1}(E_j + (n\pm 1)\hbar\omega_0) \qquad (14b)$$

By repeatedly carrying out the iteration for $m + 1$ steps, we get

$$\Phi^{m+1}(E_j + n\hbar\omega_0) = S_0^{-1}(E_j + n\hbar\omega_0)$$
$$\times[1 + S_a(E_j + n\hbar\omega_0)\Phi^m(E_j + (n+1)\hbar\omega_0)$$
$$+S_e(E_j + n\hbar\omega_0)\Phi^m(E_j + (n-1)\hbar\omega_0)]. \qquad (15)$$

The iteration is terminated for a given value of $E_{\mathbf{k}}$ when $\Phi^{m+1}(E_{\mathbf{k}})$ converges to within some preset tolerance.

2.3. Thermoelectric transport coefficients

Under the influence of a weak static electric field $\mathbf{E}$ and temperature gradient ∇T, a macroscopic electric current density $\mathbf{J}$, and heat current density $\mathbf{U}$ are produced in this medium. The perturbing function $\Phi(E_{\mathbf{k}})$, obtained above, is used in $f_1(E_{\mathbf{k}})$ to obtain $\mathbf{J}$ and $\mathbf{U}$ and in turn to find thermoelectric transport coefficients. Following Ziman [35], the thermoelectric transport coefficients in 3DDS Cd_3As_2 are given by

$$\sigma = e^2\mathbf{K}_{11} \qquad (16)$$

$$\kappa_e = \frac{1}{T}\left(\mathbf{K}_{31} - \frac{\mathbf{K}_{21}^2}{\mathbf{K}_{11}}\right) \qquad (17)$$

and

$$S^d = -\frac{1}{eT}\frac{\mathbf{K}_{21}}{\mathbf{K}_{11}} \qquad (18)$$

where

$$\mathbf{K}_{rs} = \frac{g_s g_v}{8\pi^3}\int\Phi^s(E_{\mathbf{k}})v_{\mathbf{k}}v_{\mathbf{k}}(E_{\mathbf{k}}-E_F)^{r-1}\left(\frac{\partial f_0(E_{\mathbf{k}})}{\partial E_{\mathbf{k}}}\right)\mathrm{d}\mathbf{k}. \qquad (19)$$

Table 1. The material parameters of the 3DDS Cd_3As_2.

Parameter	Value	References
High-frequency dielectric constant (ε_∞)	12	[37]
Low-frequency dielectric constant (ε_s)	36	[38]
Mass density (ρ_m)	7×10^3 kg m^{-3}	[33]
Acoustic deformation potential (D)	20 eV[a]	[29, 33]
Optical phonon energy ($\hbar\omega_0$)	25 meV	[40, 41]
Acoustic Phonon velocity (v_{ph})	2.3×10^3 m s^{-1}	[42, 43]
Fermi velocity (v_F)	10^6 m s^{-1}	[15, 18, 42]

[a] It is varied when compared with the experimental results.

Thus, once the value of perturbation function $\Phi(E_\mathbf{k})$ is obtained by the iterative technique, σ, κ_e, and S^d can be investigated numerically through K_{rs}.
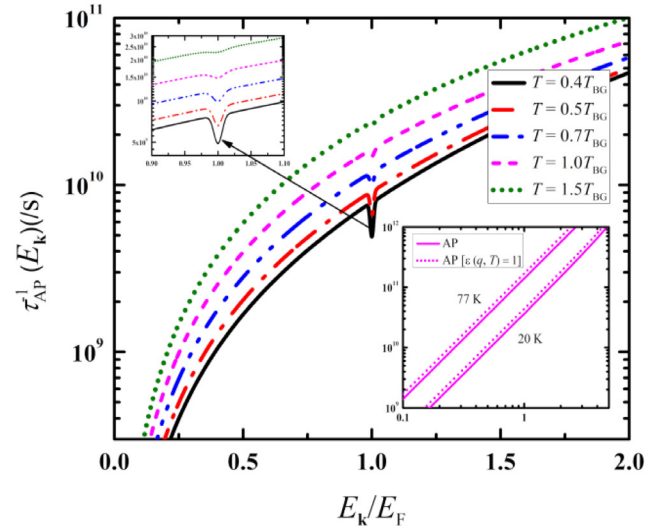
3. Results and discussion

In this section, we present the numerical calculations of perturbation function, and thermoelectric properties, using the theoretical framework given in section 2. Also, we compare our calculations with the experimental data. The material parameters of the 3DDS Cd_3As_2 used in our calculations are listed in table 1.

3.1. Temperature and electron concentration dependence

We present the calculations of the σ, κ_e and S^d as a function of temperature and electron concentration for the range $T = 2$–300 K and $n_e = (0.1$–$10) \times 10^{18}$ cm^{-3}. A reasonable value of charged impurity concentration $n_i = 1 \times 10^{18}$ cm^{-3} and $n_d V_0^2 = \hbar^2 v_F^2/q_0$ with $q_0 = 1/6$ Å [36] are chosen for illustration.

As thermoelectric properties are sensitive to the energy dependence of perturbation function $\Phi(E_\mathbf{k})$, we present its numerical evaluation for the interaction of electrons with inelastic polar optical phonons and relaxation rates for the interaction of electrons with acoustic phonons, charged impurities and short-range disorder for $n_e = 10^{18}$ cm^{-3}.

Since relaxation time due to acoustic phonon scattering is exhibiting a characteristic feature, in figure 1, we first present, $\tau_{AP}^{-1}(E_\mathbf{k})$ versus $E_\mathbf{k}/E_F$. It is shown for $T/T_{BG} = 0.4, 0.5, 0.7, 1$ and 1.5 with $T_{BG} = 8.629$ K for $n_e = 10^{18}$ cm^{-3} ($E_F \approx 162$ meV). The $\tau_{AP}^{-1}(E_\mathbf{k})$ is found to increase with the increase in carrier energy and the increase is $\sim E_\mathbf{k}^2$. The energy-dependent relaxation time shows a characteristic dip (suppression of scattering rate) at $E_\mathbf{k}/E_F = 1$ which arises due to the statistical occupation factor $[N_q f_0(E_{\mathbf{k}'}) (1 - f_0(E_\mathbf{k}) + (N_q + 1) f_0(E_\mathbf{k}) (1 - f_0 (E_{\mathbf{k}'}))]$ in the acoustic phonon relaxation time (equation (10)). The depth of the dip decreases with increase in the temperature and starts to disappear when $T/T_{BG} = 1$. The behaviour is similar to that observed in graphene (2D Dirac
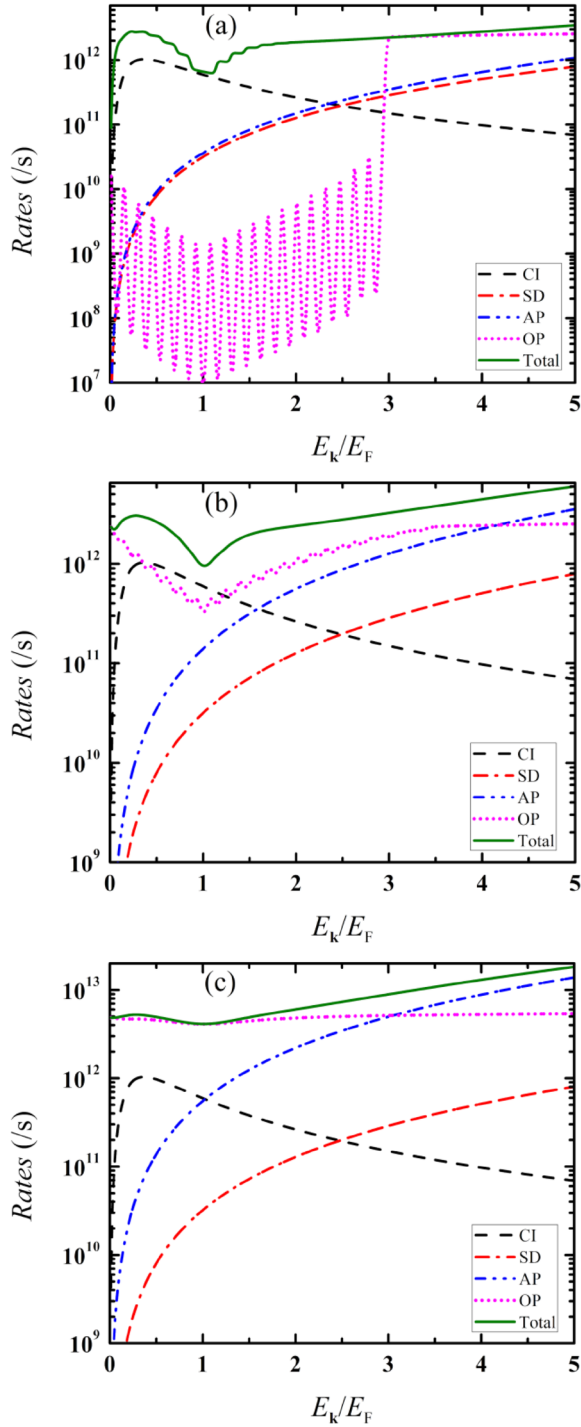

Figure 1. Inverse relaxation time due to acoustic phonon scattering as a function of electron energy for different $T/T_{BG} = 0.4, 0.5, 0.7, 1.0$ and 1.5 with $T_{BG} = 8.629$ K for an electron density $n_e = 1 \times 10^{18}$ cm^{-3}. Inset: inverse relaxation time as a function of electron energy with and without screening at 20 and 77 K.

fermions) [44], bilayer graphene (BLG) [45] and conventional 2DEG [31]. In the latter two cases, the energy dispersion relation is parabolic. The unscreened $\tau_{AP}^{-1}(E_\mathbf{k})$ as a function of $E_\mathbf{k}/E_F$ is shown in the inset for $T = 20$ and 77 K. The effect of screening is found to reduce the $\tau_{AP}^{-1}(E_\mathbf{k})$ by 1.2 times, agreeing with predictions in [29].

In order to know the relative importance of various scattering mechanisms, the relaxation rates calculated from the equations (7), (8) and (10) for the CI, SD, and AP scattering and perturbation function $\Phi(E_\mathbf{k})$ for OP scattering, using equation (15), (within 0.001% percentage of tolerance) are presented in figures 2(a)–(c) for $T = 20, 77$ and 300 K, respectively.
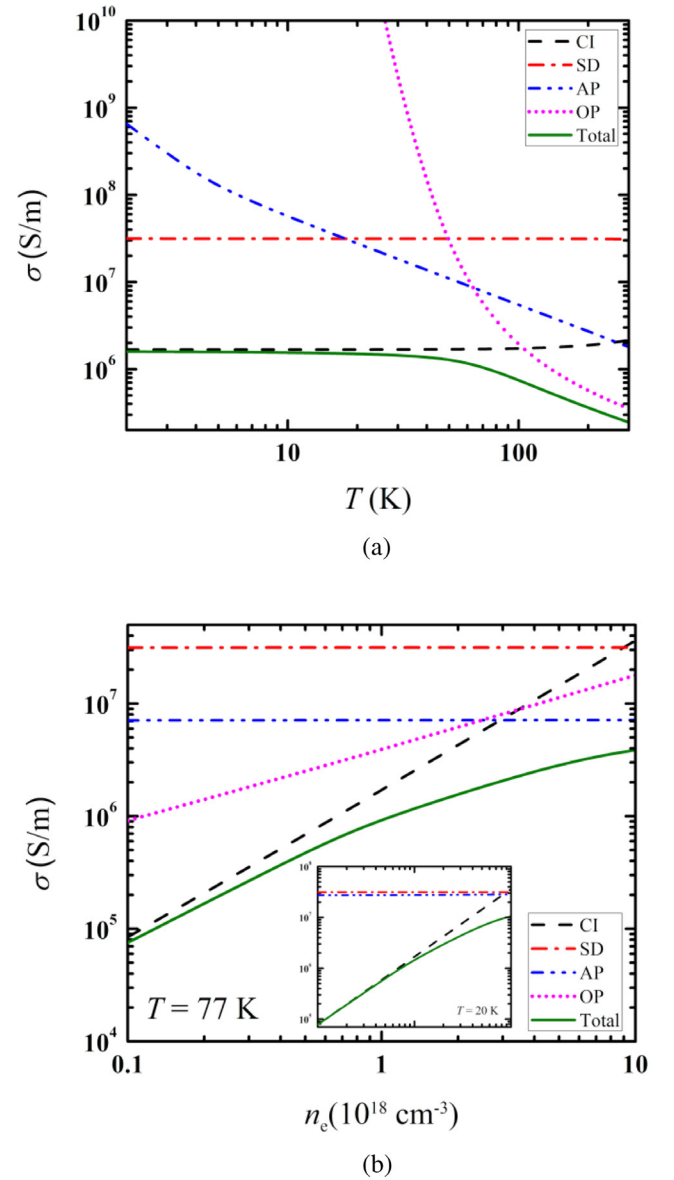
The $\Phi(E_\mathbf{k})$ is obtained by iterative procedure and the results are presented as a function of electron energy $E_\mathbf{k}$ for OP scattering in a combination of scattering from AP, CI, and SD. In the curve due to OP scattering, we observe oscillatory bumps due to the emission of phonons when the energy of the carrier is equal to $\hbar\omega_0$ and its integer multiples. These oscillatory bumps are well defined at lower carrier energy for about $E_\mathbf{k}/E_F < 2.5$ and saturate at higher energy. It is also observed that with an increase in the temperature the sharpness of the bumps keeps reducing and the curve becomes smooth. The solid curve represents the total relaxation time which is calculated by using the iterative technique including the contribution of the elastic, quasi-elastic and inelastic scattering mechanisms discussed in section 2. It can also be noticed that at $T = 20$ K (figure 2(a)) for low carrier energy $E_\mathbf{k}/E_F < \sim 2$, scattering due to CI dominates the overall rate and OP scattering dominates for $E_\mathbf{k}/E_F > \sim 2$. The oscillatory bumps that appear in the optical phonon curve are found to be reflected in the resultant curve as well. For $T > 77$ K and 300 K, the overall rate is dominated by AP and OP scattering. With increasing temperature, the oscillatory bumps gradually disappear. Also,

Figure 2. Relaxation rates as a function of electron energy due to scattering by CI, SD, AP, and perturbation function due to inelastic scattering of OP. (a) 20 K, (b) 77 K and (c) 300 K.

we have observed that the relaxation time due to CI is independent of temperature. The contribution from SD is found to be negligible.
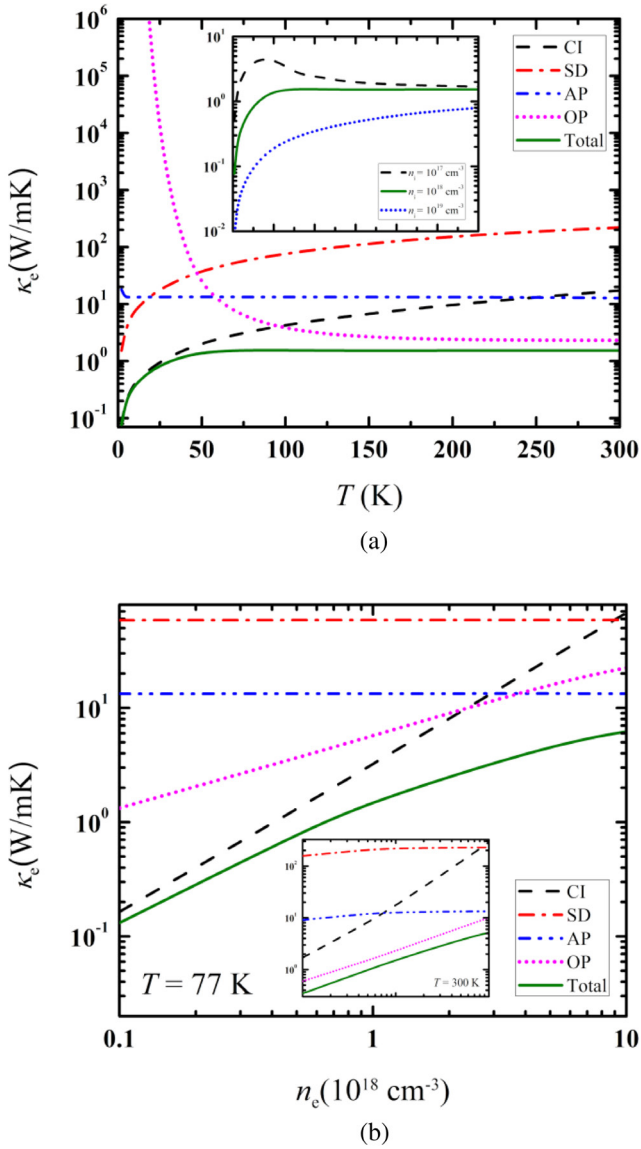
In figure 3(a), we present the calculations of σ as a function of T, evaluated for $n_e = 1 \times 10^{18}$ cm^{-3}. For the n_i chosen, scattering due to CI is dominant for about $T < 70$ K making the overall σ to be almost independent of temperature in this region. For $T > 70$ K scattering due to optical phonons becomes dominant and σ decreases with increasing T.

Figure 3. (a) The electrical conductivity as a function of temperature for scattering due to CI, SD, AP, OP and resultant of all these mechanisms for $n_e = 1 \times 10^{18}$ cm^{-3} and $n_i = 1 \times 10^{18}$ cm^{-3}. (b) Electrical conductivity as a function of electron concentration at $T = 77$ K. Inset: at $T = 20$ K.

Moreover, the contribution from AP scattering is found to be considerable for about $T > 40$ K.

In figure 3(b), the calculations are shown for σ as a function of n_e, at 77 K. The σ due to CI (phonon) scattering is increasing with increasing n_e as $\sigma \sim n_e^{1.3(0.6)}$. The n_e dependence of σ due to AP is found to be stronger than that due to OP scattering and also SD is independent of carrier concentration. It is seen that for low n_e ($< \sim 2.5 \times 10^{18}$ cm^{-3}) contribution due to the CI dominates over the contribution from the phonon scattering. At higher n_e, we see that overall σ is found to increase and APs dominate the carrier scattering at higher concentration, at this temperature. At 20 K (inset figure) σ is dominated by CI for about n_e up to 7.0×10^{18} cm^{-3}. The variation of σ due to CI is $\sigma \sim n_e^{1.3}$. For $n_e > 7.0 \times 10^{18}$ cm^{-3}, the contribution from AP

Figure 4. (a) The electronic thermal conductivity as a function of temperature due to scattering by CI, SD, AP and OP and the resultant of all these mechanisms for $n_e = 1 \times 10^{18}$ cm^{-3} and $n_i = 1 \times 10^{18}$ cm^{-3}. Inset: the resultant electronic thermal conductivity as a function of temperature with $n_i = 0.1, 1, 10 \times 10^{18}$ cm^{-3}. (b) Electronic thermal conductivity as a function of electron concentration at $T = 77$ K. Inset: at $T = 300$ K.

scattering dominates total σ. Consequently, total σ versus n_e shows maximum for $n_e = 10 \times 10^{18}$ cm^{-3}.

The calculations of electronic thermal conductivity κ_e as a function of temperature T for $n_e = 1 \times 10^{18}$ cm^{-3} and $n_i = 1 \times 10^{18}$ cm^{-3} are presented in figure 4(a). The contribution for κ_e from the individual scattering mechanisms (CI, SD, AP, and OP) are presented using the respective relaxation times to see the relative significance. For about $T < 75$ K, the total κ_e is dominated by contribution due to CI and for $T > 75$ K the total κ_e is dominated by the contribution from OP scattering. For about $T > 30$ K, the contribution from AP scattering is significant, although it is not dominant. For $T < 30$ K, the total κ_e found to increase linearly ($\sim T$) with temperature (found by curve fit, although it is not obvious in the semi log

scale of figure 4(a)) and it is only due to the scattering by CI. This observation validates Wiedemann–Franz law that (κ_e/σ) $\sim T$, as σ due to CI, in this temperature range, is independent of T (as seen from figure 3(a)). For about $30 < T < 70$ K, the total κ_e found to increase sub-linearly ($\sim T^{0.5}$). In the higher temperature region ($T > 70$ K) the total κ_e found to be independent of T. This may be ascribed to the fact that σ, due to phonon scattering, is decreasing with increasing T and the product σT is nearly independent of temperature. This range will shift to lower (higher) temperature region (seen in the inset) with the decrease (increase) of impurity concentration. Obviously, it is attributed to the shift in the CI dominating region of temperature. A very weak T dependence of κ_e for $T > 100$ K is nearly validating the Wiedemann–Franz law for optical phonons scattering.
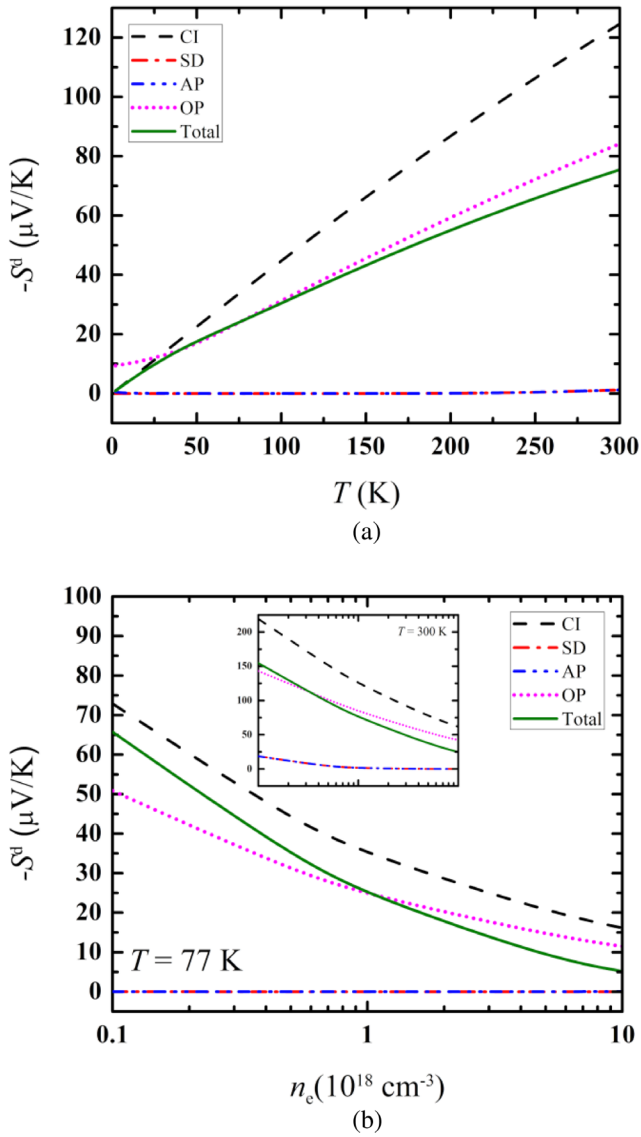
In figure 4(b), we present the calculations of κ_e as a function of n_e at 77 K (inset: 300 K). At 77 K, it is found that scattering due to CI found to dominate the κ_e at lower carrier concentration ~ 0.1–1.0×10^{18} cm^{-3}, and at higher n_e, the scattering by phonons limit the κ_e. It is found that κ_e due to AP and SD is almost independent of n_e and AP scattering is found to dominate in the high n_e region. At 300 K, OP found to dominate the κ_e in the entire n_e range. The total κ_e is found to increase as $\sim n_e^{1(0.6)}$ at 77 K (300 K) in the considered range of n_e.

The temperature dependence of diffusion thermopower S^d is shown in figure 5(a) for $2 < T < 300$ K. The curves are shown for individual scattering due to CI, SD, AP, and OP in order to see their relative contribution to the resultant S^d. The S^d due to CI scattering coincides with the total curve at lower temperature $T < 20$ K. It can also be seen from the energy dependence of the relaxation time in figure 2(a). At higher T, the S^d due to CI and OP scattering mechanisms are large compared to the total S^d. However, for $T > \sim 50$ K the resultant S^d is mainly controlled by the OP scattering and the contribution from CI scattering is small, consistent with the energy dependence of the relaxation time calculations. The resultant S^d shows a linear behaviour for $T < 20$ K and becomes nearly linear at higher T. This is comparable to the observation made in MLG [46] and BLG [45].

We present the n_e dependence of diffusion thermopower S^d at 77 K (inset: 300 K) in figure 5(b). At 77 K, for low $n_e \sim 0.1$–1×10^{18} cm^{-3} scattering by CI is found to dominate the overall thermopower showing $S^d \sim n_e^{-0.3}$. At higher n_e, OP scattering is found to limit S^d showing $n_e^{-0.3}$ dependence. The overall S^d is found to decrease as $\sim n_e^{-0.4}$. At 300 K, scattering due to OP is found to dominate S^d and resultant is found to decrease as $\sim n_e^{-0.4}$. The results observed by us are in agreement with the Mott formula ($S^d \sim E_F^{-1} \sim n_e^{-1/3}$) and also with the calculations presented by Pariari *et al* [27] while explaining their observed experimental results. Relaxation time due to SD varies as E_k^{-2} giving its zero contribution to S^d.

3.2. Comparison with experiment

In the following, with our calculations, we have explained the experimental results of resistivity [12, 15, 18], thermal conductivity [25, 26] and thermopower [26, 27] using respective

Figure 5. (a) The diffusion thermopower as a function of temperature for scattering due to CI, SD, AP, OP and resultant of all these mechanisms for $n_e = 1 \times 10^{18}$ cm^{-3} and $n_i = 1 \times 10^{18}$ cm^{-3}. (b) Diffusion thermopower as a function of electron concentration at $T = 77$ K. Inset: at $T = 300$ K.

material parameters of these samples. In order to explain these data, since the CI concentration n_i are not given, we vary it to fit the very low temperature experimental data. Also, acoustic deformation potential constant D is varied, in the range (10–30 eV [29, 33]), to fit the data at intermediate temperature.

In figure 6(a), we have shown the comparison of our calculations with experimentally measured ρ of Liang *et al* [15]. The authors have measured ρ as a function of temperature in the range ~2–200 K for $n_e = 1.33 \times 10^{19}$ cm^{-3} (sample-B1) and 1.5×10^{19} cm^{-3} (sample-B7). For sample-B1, the experimental data shows the residual resistivity $\rho_0 = 46.5$ $\mu\Omega$ cm at very low T (~5 K). The charged impurity concentration $n_i = 2 \times 10^{19}$ cm^{-3} is chosen to obtain this residual resistivity. Then, $D = 29.7$ eV is chosen to fit experimental data in the intermediate temperature region. We have shown ρ due to CI, SD, AP and OP and their total. A good agreement of resultant

ρ is obtained with the experimental results in the entire temperature range. In the inset, we have shown the calculations for the sample B7 with $n_e = 1.5 \times 10^{19}$ cm^{-3}, by choosing $n_i = 1.56 \times 10^{19}$ cm^{-3} and $D = 28.2$ eV in order to explain the observed results. It was found that, in both samples, at low temperature CI scattering dominates the overall ρ and at higher temperature scattering due to APs dominates [11, 42].
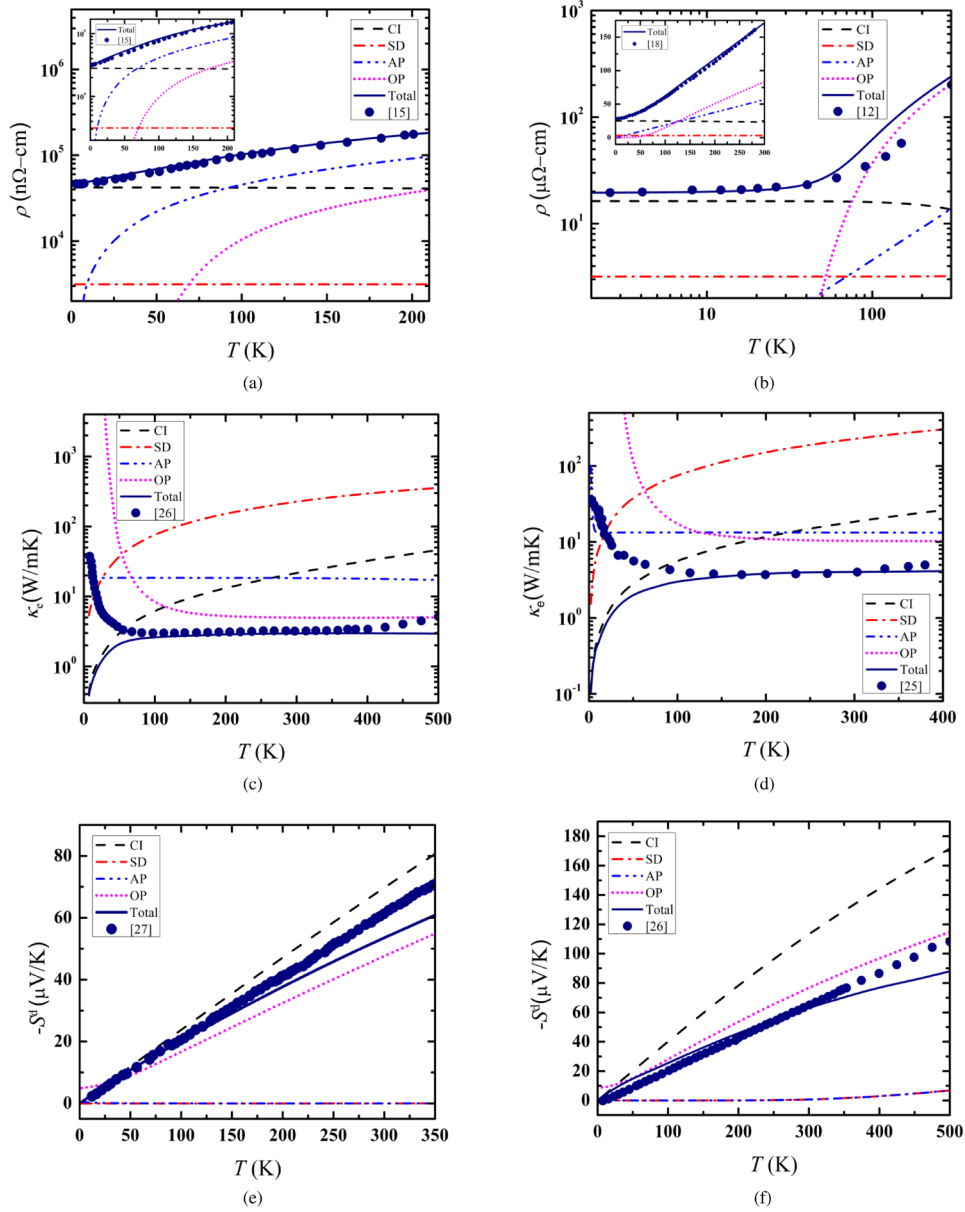
We perform the resistivity calculations for the sample of Cao *et al* [12] with $n_e = 1.67 \times 10^{18}$ cm^{-3} and compare with their experimental results in figure 6(b). We vary the deformation potential constant to $D = 10$ eV and the impurity concentration to $n_i = 5.41 \times 10^{17}$ cm^{-3} to match with the experimental data. There is a good agreement for $T < 60$ K, the region where CI scattering dominates the overall mobility. At higher temperature, the theoretical curves are larger than the observed results to some extent. In this temperature region OP scattering dominates the resultant resistivity. Similar observation is made by Kubakaddi in the phonon limited mobility study in which scattering by OPs is taken in the quasi-elastic approximation [29]. Along with the resultant curve, we have shown contributions from individual scattering mechanisms. In the inset, we show ρ versus T (~2–300 K) for the sample of He *et al* [18] with $n_e = 5.3 \times 10^{18}$ cm^{-3}. We find that, following the same procedure as mentioned above, the choice of $n_i = 4.47 \times 10^{18}$ cm^{-3} and $D = 22.2$ eV gives a good agreement with experimental data. It is consistent with the mobility calculations taking the phonon scattering in the quasi-elastic approximation [29]. It is again found that CI scattering dominates the ρ at low T and optical phonon scattering limit the ρ at higher T.

In the following, while explaining the thermal conductivity and thermopower data, we obtain n_i in the respective samples by fitting to their residual resistivity/mobility. Then, deformation potential constant D is varied to obtain the agreement with the experimental data.

A comparison of thermal conductivity as a function of temperature for the sample D of Wang *et al* [26] with $n_e = 3.3 \times 10^{18}$ cm^{-3} in the temperature range ~7–500 K is presented in figure 6(c). The experimentally measured thermal conductivity has the contributions from both the electronic and phonon part, $\kappa = \kappa_e + \kappa_{ph}$. Although the phonon contribution κ_{ph} to κ is the dominant at low T, we attempt to explain the results only for $T > $ ~50 K with the electronic contributions. The choice of $n_i = 3.29 \times 10^{18}$ cm^{-3} will give the residual resistivity 39.9 $\mu\Omega$ cm of this sample. Then choosing $D = 17$ eV, we obtain a reasonably good agreement with the observed results. By using the above parameters, we give the calculations of κ_e as a function of T for the individual mechanisms to measure their relative contribution to the total κ. For $T > 100$ K we found the total curve being dominated by the electron scattering from phonons.

The calculations of κ_e as a function of temperature are carried out for the sample of Zhang *et al* [25] with $n_e = 1 \times 10^{19}$ cm^{-3} and residual resistivity 46.22 $\mu\Omega$ cm and compared with their experimental data in figure 6(d). The residual resistivity in this sample can be obtained by selecting $n_i = 1.67 \times 10^{19}$ cm^{-3}. Then experimental observations of κ are explained with

Figure 6. (a) Resistivity ρ as a function temperature T for the sample B1 (B7-Inset) of Liang *et al* [15]. The curves represent the calculated ρ due to CI, SD, AP, OP and the resultant ρ. The solid circles represent the experimental data. (b) Resistivity ρ as a function of temperature for the sample of Cao *et al* [12]. The curves represent the calculated ρ due to CI, SD, AP, OP and the resultant ρ. Inset: ρ as a function of temperature T is shown for the sample of He *et al* [18]. The solid circles represent the experimental data. (c) Thermal conductivity κ as a function temperature T for the sample D of Wang *et al* [26]. The curves represent the calculated κ_e due to CI, SD, AP, OP and the resultant κ_e. The solid circles represent the experimental data. (d) Electronic thermal conductivity κ_e as a function temperature T for the sample of Zhang *et al* [25]. The curves represent the calculated κ_e due to CI, SD, AP, OP and the resultant. The solid circles represent the experimental data. (e) Thermopower S^d as a function of temperature for the sample of Pariari *et al* [27]. The curves represent the calculated S^d due to CI, SD, AP, OP and the resultant S^d. The solid circles represent the experimental data. (f) Thermopower S^d as a function of temperature for the sample C of Wang *et al* [26]. The curves represent the calculated S^d due to CI, SD, AP, OP and the resultant S^d. The solid circles represent the experimental data.

$D = 20\,\text{eV}$. For $T > \sim 200\,\text{K}$ scattering from APs and OPs is found to dominate κ_e.

At low temperature, the thermal conductivity κ is generally dominated by phonon thermal conductivity κ_{ph} in large n_e samples [22]. This κ_{ph} arises due to phonon scattering by (i) boundary ($\kappa_{ph\text{-}b}$) at very low T, (ii) phonons ($\kappa_{ph\text{-}ph}$), (iii) impurities ($\kappa_{ph\text{-}i}$) and (iii) point defects ($\kappa_{ph\text{-}d}$), at relatively higher T. Resultant κ_{ph} is given by $1/\kappa_{ph} = (1/\kappa_{ph\text{-}b}) + (1/\kappa_{ph\text{-}ph}) + (1/\kappa_{ph\text{-}i}) + (1/\kappa_{ph\text{-}d})$. It is found that $\kappa_{ph\text{-}b} \sim T^3$ and other

mechanisms together show $\kappa_{ph} \sim T^{-1}$, dominated by $\kappa_{ph\text{-}ph}$. We believe that in figures 6(c) and (d), the low T data (below 50 K), but not very low T, is governed by the $\kappa_{ph} \sim T^{-1}$ behaviour which is due to the phonon scattering by phonons, impurity, and defects. In 3D Cd$_3$As$_2$ semiconductor, it has been shown that lattice thermal conductivity, with a peak at 8 K, is decreasing with increasing temperature nearly as T^{-1} [47, 48]. In order to make a quantitative comparison with the experimental data for $T < 50\,\text{K}$, one needs to obtain $\kappa_{ph\text{-}b}$, $\kappa_{ph\text{-}i}$,

$\kappa_{\text{ph-ph}}$ and $\kappa_{\text{ph-d}}$, by solving the phonon BTE in the relaxation time approximation in 3DDS. It is out of scope of the present work.

Pariari *et al* [27] have made the temperature-dependent measurements of Seebeck coefficient S^d in the range ~2–350 K in zero and quantizing magnetic field. In figure 6(e), we attempt to explain their zero-field thermopower data (from figure 4(a) of [27]). From the Hall resistivity measurements, the electron concentration of the sample is found to be $n_e = 6.8 \times 10^{18}$ cm^{-3}. The charged impurity concentration $n_i = 1.52 \times 10^{19}$ cm^{-3} is chosen to fit the residual mobility of the sample ~1.3×10^4 cm^2 V^{-1} s^{-1} at $T = 2$ K. Also, we chose $D = 5$ eV to obtain agreement between the calculated S^d and the experimental data. By using these values of n_i, n_e and D, we present the calculations of S^d as a function T. The calculations best fit the data up to 200 K. The calculations of S^d for individual scattering mechanisms are also presented to gauge their relative importance. It is clear that overall thermopower for $T < $ ~20 K is dominated by scattering from CIs and at higher T by OPs.

Wang *et al* [26] have made the temperature-dependent measurements of Seebeck coefficient in the range ~6–500 K in zero magnetic field. In figure 6(f), we attempt to explain their zero-field thermopower data with our calculations for the sample C with $n_e = 1.39 \times 10^{18}$ cm^{-3} and the residual resistivity 58.7 $\mu\Omega$ cm. This value of residual resistivity can be obtained by choosing of $n_i = 1.52 \times 10^{18}$ cm^{-3}. Then, $D = 25$ eV is chosen to explain the observed thermopower data. The calculations give reasonably good agreement with the data up to 350 K and it deviates marginally at a higher temperature.

From the comparison of the experimental results of σ, κ, and S, it can be seen that scattering by charged impurities is sufficient to explain the observed transport properties of the Cd$_3$As$_2$ at low temperature. The phonon scattering limits the transport in higher temperature region.

We would like to make the following remarks regarding n_i. While comparing with the experimental data, n_i is used as fitting parameter at very low T, where $\sigma = \sigma_{\text{CI}}$ is independent of T. The n_i thus used is believed to be sample specific due to its preparation and it is found to be in the same range as that of n_e. The use of n_i in the range of n_e, and sometimes $n_i > n_e$, is also found in some earlier works [49, 50]. We have found that theoretical residual resistivity $\rho = \rho_{\text{CI}}$ ($=\sigma_{\text{CI}}^{-1}$) ~ ($n_i/n_e^{1.3}$). Interestingly, it is also noticed that, taking $n_r = (n_i/n_e^{1.3})$, the ratio of n_r's of any two of the experimental samples, considered here, is nearly equal to the ratio of their respective experimental residual resistivities. Moreover, in the samples with nearly same residual resistivity, sample with larger n_e is found to have larger n_i, because ρ_{CI} ~ ($n_i/n_e^{1.3}$). These may reflect a kind of consistency in our choice of n_i for samples with different residual resistivity and n_e. Additionally, it is also noticed that, in the samples with residual resistivity of the order of few tens of $\mu\Omega$ cm, the required n_i is about 2–4 orders of magnitude larger, depending upon n_e value, than the n_i required in samples of few tens of nΩ cm of residual resistivity (sample of Zhao *et al* [14] and samples A1, A5 and

A8 of Liang *et al* [15]), suggesting that the latter samples are nearly clean samples.

4. Conclusions

In conclusion, thermoelectric properties of 3DDS Cd$_3$As$_2$ are theoretically investigated as a function of temperature T and electron concentration n_e by considering the electron scattering from the charged impurity, short-range disorder, acoustic and optical phonons. The first-order perturbation $\Phi(E_{\mathbf{k}})$ of the distribution function has been presented as a function of carrier energy $E_{\mathbf{k}}$ for the inelastic polar optical phonons, along with other elastic scattering processes, which is obtained by solving the linearized BTE via Ritz iteration method. At low temperatures, our results show that all thermoelectric transport properties (σ, κ_e, S^d) are dominated by the scattering of CIs. In the numerical calculations, at low temperature, we have found σ to be almost independent of temperature and the residual resistivity $\rho = \rho_{\text{CI}}$ is shown to be ~ ($n_i/n_e^{1.3}$). At a higher temperature, it decreases with an increase of T due to the influence of phonon scattering. At lower temperature κ_e was found to increase linearly with temperature dominated by CI scattering and is almost independent of temperature at higher T. The Wiedemann–Franz law (κ_e/σ) ~ T is largely validated for CI and phonon scattering. The diffusion thermopower S^d, in the low temperature region, was found to be linear in T and dominated by CIs scattering. With the increasing temperature, S^d is nearly linear in T due to the dominance of scattering from phonons. S^d results are in agreement with the Mott's relation at low T. The experimental data of ρ, κ and S are explained, by varying deformation potential constant D in the range 10–30 eV.

Note

After completion this work, we became aware of a recent work [51], in which the calculated lattice thermal conductivity κ_{ph} in the Dirac semimetal Cd$_3$As$_2$ at 300 K is found to be in the range of 0.3–0.9 W/mK and it is decreasing with increasing T. These authors claim that their predictions are in good agreement with the experimental reports of Wang *et al* [52]. However, the observed thermal conductivity in [52], in the temperature range of 100–400 K, is $\sim$ 3 W/mK and is almost independent of T. Our calculations of κ_e are in good agreement with these experimental reports of [52], as found with the data in [26] by the same group (figure 6(c)).

ORCID iDs

K S Bhargavi ⓘ https://orcid.org/0000-0002-7087-8578
S S Kubakaddi ⓘ https://orcid.org/0000-0002-4702-868X

References

[1] Geim A K and Novoselov K S 2007 *Nat. Mater.* **6** 183
[2] Sarma S D, Adam S, Hwang E H and Rossi E 2011 *Rev. Mod. Phys.* **83** 407
[3] Young S M, Zaheer S, Teo J C Y, Kane C L, Mele E J and Rappe A M 2012 *Phys. Rev. Lett.* **108** 140405
[4] Wang Z, Sun Y, Chen X Q, Franchini C, Xu G, Weng H, Dai X and Fang Z 2012 *Phys. Rev. B* **85** 195320
[5] Singh B, Sharma A, Lin H, Hasan M Z, Prasad R and Bansil A 2012 *Phys. Rev. B* **86** 115208
[6] Wang Z, Weng H, Wu Q, Dai X and Fang Z 2013 *Phys. Rev. B* **88** 125427
[7] Armitage N P, Mele E J and Vishwanath A 2018 *Rev. Mod. Phys.* **90** 015001
[8] Liu Z K *et al* 2014 *Nat. Mater.* **13** 677–81
[9] Borisenko S, Gibson Q, Evtushinsky D, Zabolotnyy V, Buchner B and Cava R J 2014 *Phys. Rev. Lett.* **113** 027603
[10] Lundgren R, Laurell P and Fiete G A 2014 *Phys. Rev. B* **90** 165115
[11] Sarma S D, Hwang E H and Min H 2015 *Phys. Rev. B* **91** 035201
[12] Cao J *et al* 2015 *Nat. Commun.* **6** 7779
[13] Jin H, Dai Y, Ma Y D, Li X R, Wei W, Yu L and Huanga B B 2015 *J. Mater. Chem. C* **3** 3547
[14] Zhao Y *et al* 2015 *Phys. Rev. X* **5** 031037
[15] Liang T, Gibson Q, Ali M N, Liu M, Cava R J and Ong N P 2015 *Nat. Mater.* **14** 280–4
[16] Neupane M *et al* 2014 *Nat. Commun.* **5** 3786
[17] Narayanan A *et al* 2015 *Phys. Rev. Lett.* **114** 117201
[18] He L P, Hong X C, Dong J K, Pan J, Zhang Z, Zhang J and Li S Y 2014 *Phys. Rev. Lett.* **113** 246402
[19] Conte A M, Pulci O and Bechstedt F 2017 *Sci. Rep.* **7** 45500
[20] Feng J, Pang Y, Wu D, Wang Z, Weng H, Li J, Dai X, Fang Z, Shi Y and Lu L 2015 *Phys. Rev. B* **92** 081306
[21] Mahan G D 1998 Good thermoelectrics *Solid State Physics* vol 51, ed H Ehrenreich and F Spaefen (New York: Academic) p 81
[22] Rowe D M (ed) 2006 *Thermoelectrics Handbook—Macro to Nano* (Boca Raton, FL: CRC Press)
[23] Gooth J, Schierning G, Felser C and Nielsch K 2018 *MRS Bull.* **43** 187–92
[24] Mulla R and Dunnill C W 2019 *ChemSusChem* **12** 3882–95
[25] Zhang C *et al* 2015 *Chin. Phys. B* **25** 017202
[26] Wang H *et al* 2019 *Adv. Funct. Mater.* 1902437
[27] Pariari A, Khan N, Singha R, Satpati B and Mandal P 2016 *Phys. Rev. B* **94** 165139
[28] Zhou T, Zhang C, Zhang H, Xiu F and Yang Z 2016 *Inorg. Chem. Frontiers* **3** 1637
[29] Kubakaddi S S 2019 *J. Appl. Phys.* **126** 135703
[30] Nag B R 1980 *Electron Transport in Compound Semiconductors* (*Springer Series in Solid-State Sciences* vol 11) ed M Cardona *et al* (New York: Springer)
[31] Kawamura T and Sarma S D 1992 *Phys. Rev. B* **45** 3612
[32] Gantmakher V F and Levinson Y B 1987 *Carrier Scattering in Metals and Semiconductors* (Amsterdam: Elsevier)
[33] Jay-Gerin J P, Aubin M J and Caron L G 1978 *Phys. Rev. B* **80** 4542
[34] Basu P K and Nag B R 1980 *Phys. Rev. B* **22** 4849
[35] Ziman J M 1972 *Principles of the Theory of Solids* 2nd edn (Cambridge: Cambridge University Press)
[36] Shao J M and Yang G W 2015 *AIP Adv.* **5** 117213.
[37] Jay-Gerin J P, Caron L G and Aubin M J 1977 *Can. J. Phys.* **55** 956
[38] Jay-Gerin J P, Aubin M J and Caron L G 1977 *Solid State Commun.* **21** 771
[39] Kubakaddi S S and Biswas T 2018 *J. Phys.: Condens. Matter* **30** 265303
[40] Weszka J 1999 *Phys. Status Solidi* b **211** 605
[41] Lu W, Ge S, Liu X, Lu H, Li C, Lai J, Zhao C, Liao Z, Jia S and Sun D 2017 *Phys. Rev. B* **95** 024303
[42] Lundgren R and Fiete G A 2015 *Phys. Rev. B* **92** 125139
[43] Wang H, Xu Y, Shimono M, Tanaka Y and Yamazaki M 2007 *Mater. Trans.* **48** 2349
[44] Hwang E H and Sarma S D 2008 *Phys. Rev. B* **77** 115449
[45] Bhargavi K S and Kubakaddi S S 2013 *Physica* E **52** 116–21
[46] Kubakaddi S S 2009 *Phys. Rev. B* **79** 075417
[47] Armitage D and Goldsmid H J 1969 *J. Phys. C: Solid State Phys.* **2** 2138
[48] Bartkowski K, Rafalowicz J and Zdanowicz W 1986 *Int. J. Thermophys* **7** 765
[49] Cao J, Querales-Flores J D, Murphy A R, Fahy S and Savić I 2018 *Phys. Rev. B* **98** 205202
[50] Ma N and Jena D 2014 *Phys. Rev. X* **4** 011043
[51] Yue S, Chorsi H T, Goyal M, Schumann T, Yang R, Xu T, Deng B, Stemmer S, Schuller J A and Liao B 2019 *Phys. Rev. Research* **1** 033101
[52] Wang H, Luo X, Chen W, Wang N, Lei B, Meng F, Shang C, Ma L, Wu T and Dai X 2018 *Sci. Bull.* **63** 411